The influence of advanced hot isostatic pressing on phase transformations, mechanical properties of Ti-34Nb-13Ta-5Zr-0.2O alloy manufactured by In-situ alloying via selective laser melting

Weihuan Kong[a], Elisabeth M. Francis[b], Qi Shi[c], Sophie C. Cox[d], Feng Wang[a], Min Kuang[c], Moataz M. Attallah[a,*]

[a] School of Materials and Metallurgy, University of Birmingham, Edgbaston B15 2TT, UK
[b] Manchester Materials Science Centre, The University of Manchester, Grosvenor Street, Manchester M1 7HS, UK
[c] Guangdong Institute of New Materials, Guangdong Academy of Science, Guangzhou 510651, PR China
[d] School of Chemical Engineering, University of Birmingham, Edgbaston B15 2TT, UK

ARTICLE INFO

ABSTRACT

In this paper, advanced hot isostatic pressing (HIP) subjected to high and intermediate cooling rate (HCR & ICR) were exploited to close keyholes and tune the microstructure of SLMed Ti-34 Nb-13Ta-5Zr-0.2 O alloys (TNT5Zr-0.2 O, wt%). XRD analysis along with SEM and TEM micrographs reveal single beta phase in grain matrix of as-fabricated TNT5Zr-0.2 O (TNT5Zr-0.2 O-AF), TNT5Zr-0.2 O-HCR, TNT5Zr-0.2 O-ICR alloys. Additionally, high-angle annular dark-field (HAADF) micrographs show discrete large Ti-rich α grain boundary precipitates in TNT5Zr-0.2 O-ICR alloy. Tensile properties show that TNT5Zr-0.2 O-AF alloy possessed high UTS of 975 ± 12 MPa, and elongation of 4.9% ± 0.3%; the TNT5Zr-0.2 O-ICR alloy obtained slightly higher UTS (1036 ± 26 MPa) and lower elongation (3.0% ± 0.3%). S-N curves demonstrate fatigue limit of TNT5Zr-0.2 O-ICR alloy (150 MPa) is slightly higher than the counterpart of TNT5Zr-0.2 O-AF alloy (130 MPa), and slip-band cracking phenomenon was observed in both alloys. Advanced HIP subjected to intermediate cooling rate functions well to close SLM-processed keyholes but the resistance to fatigue is not markedly enhanced; the addition of proper amount oxygen interstitial solutes in TNTZ-O alloy is regarded as an inexpensive, effective strengthening technique for load-bearing biomedical applications.

1. Introduction

Ti-Nb-Ta-Zr (TNTZ) alloy possesses excellent mechanical properties, such as ultralow Young's modulus, relative high strength and good plasticity, which exhibits its potential to be the next generation load-bearing implant material [1]. However, there still have some controversial microstructural evolution mechanisms in TNTZ alloys manufacturing. For example, the mechanism of oxygen effect on the phase transformation in TNTZ-O alloy (Gum Metal) is not commonly accepted. Some researchers believe that oxygen addition retards the formation of athermal ω and α'' phases in Gum Metal. Tane et al. [2,3] manufactured solution treated single crystal samples of Ti-36 Nb-2Ta-3Zr alloys containing 0.09, 0.36, 0.51 wt% oxygen and the cold-worked same metallic element composition alloy containing 0.06, 0.30, 0.47 wt% oxygen, and observed the microstructures with a TEM

equipped with cooling stage. They concluded that higher oxygen addition in different-method prepared alloys variously suppresses the formation of athermal ω and α'' phases cooling from room temperature to a fairly low temperature of ~ 13 K. Wei et al. [4] carried out TEM investigations of solution treated Ti-23 Nb-2Zr-0.7Ta-(0.6–1.8)O (at%) alloys and observed SAD patterns belonging to athermal ω phases in the three alloys. The researchers insisted that the intensity of these diffraction spots corresponding to athermal ω phases decreased with increasing oxygen concentration, which agrees with the conclusion drew from the former work. In addition, Saito et al. [5] asserted that oxygen function as interstitial atoms in Ti-23 Nb-0.7Ta-2Zr-(0.5–2.5)O (at%) alloys, then tend to form extremely short-range atom clusters around zirconium atoms, which could effectively inhibit dislocation activity. Moreover, Yokota et al. [6] observed gradient tensile strength increase in water-quenched Ti–35Ta-O alloys (at%) when oxygen content was increased from 1.5% to 4.6%. The oxygen solid solution strengthening was supported by first-principles calculations due to the existence of O atoms at the

octahedral interstitial sites in the bcc structures. Similarly, the interstitial oxygen in water-quenched Ti-(15−34)Nb-O (wt%) alloys was believed to produce a strong influence on strength and microhardness increase [7,8]. Niinomi et al. [9] questioned the conventionally accepted understanding that oxygen destabilizes the omega phase in Gum Metal. In their study, they prepared Ti-29 Nb-13Ta-4.6Zr alloys containing 0.1 and 0.4 wt% oxygen using two-step aging treatment. After performing TEM characterization, clear diffraction patterns of isothermal α'' in the former alloy and additional ω also α'' in the latter alloy were revealed. Additionally, reconstructed APT data showed that oxygen content was significantly higher in ω or α'' particle than β phase in TNTZ-0.4 O alloy. Thus, the high concentration of oxygen within that alloy was considered as the potential driving force for $\beta \rightarrow$ isothermal ω phase transformation during aging at 723 K.

The prior investigations have shown that the microstructure of high β stabilized TNT(Z) alloys is sensitive to cooling rate after the homogenization treatment. Tang et al. [10] exhibited the TEM micrographs of Ti-23.2 Nb-22.0Ta alloy (wt%), which homogenized at 1000 °C for 2 h followed by water quenching and air cooling, respectively. According to BF-TEM image and its SAD pattern, the authors asserted that martensite phases with an acicular morphology and indistinguishable embryo ω precipitates were retained in beta grain matrix after water quenching. By comparison, TEM observation indicated that the ω phase underwent a significantly growth during the slower air-cooling process. In addition to microstructure difference in the beta grain matrix caused by cooling rate, grain boundary is also regarded as a preferred site to form cooling rate dependent microstructure. Banerjee et al. [11], Nag et al. [12] both observed relatively large beta grains with grain boundary α precipitates in Ti-34 Nb-9Zr-8Ta alloy (wt%), which was homogenized at 1100 °C for 7 days then furnace cooled. Microstructural evolution and mechanical properties of Ti-29 Nb-13Ta-4.6Zr alloy (wt%) experienced solution treatment and cooling procedure via different mediums e.g. water, static air, vacuum furnace, etc was preliminarily investigated by Najdahmadi et al. [13]. Based on the measured elongation values, the furnace cooled specimen possessed the lowest ductility. The authors concluded that the formation of intergranular and intragranular precipitates in the furnace cooled TNTZ alloy leads to an inhomogeneous deformation and easier crack initiation.

In our study, we investigated the microstructural evolution, mechanical properties of SLMed Ti-34 Nb-13Ta-5Zr-0.2 O alloy (wt%) before and after advanced HIP subjected to high and intermediate cooling rate. The effect of oxygen on the microstructure, tensile and fatigue characteristics of the as-SLMed Ti-34 Nb-13Ta-5Zr-0.2 O alloy was studied. Furthermore, advanced HIP technique was exploited aiming to close the as-fabricated pores and tune the microstructure of the β Ti alloy cooled from the temperature above beta transus to room temperature.

2. Materials and methods

2.1. Powder feedstock preparation

Pure element powder was used to blend the as-designed Ti-34 Nb-13Ta-5Zr alloy (TNT5Zr, wt%) for in-situ alloying via SLM. Spherical Ti and Zr powders (TLS, Germany) with nominal particle size distribution of 15−83 µm (D50 = 38 µm)and 10−45 µm (D50 =38 µm), respectively were gas atomized in an argon atmosphere. Irregular-shaped Nb (Elite, UK), Ta powder (H.C. Starck, Germany) with an average particle size (D50) of 43.9 µm and 23.4 µm, respectively were manufactured through hydride-dehydride technique (Fig. 1 A). The mass of each elemental powder was measured using a top pan balance (Kern EMB2000, 0.01 g accuracy) inside a glove box (Saffron, UK) with an argon protective atmosphere (≤0.005% O_2). Then the powder was mixed for ten hours in a

horizontal rotating drum (Kimber-Allen, UK), and the blended powder was demonstrated by benchtop SEM (TM3030, Hitachi) (Fig. 1B).

2.2. Selective laser melting

An M2 Cusing SLM system (Concept Laser, GE Additive) was used to fabricate TNT5Zr samples on a Ti-alloy substrate. This machine was equipped with a 400 W Yb:YAG fiber laser at a wavelength of 1064 nm with a spot size of approx. 63 µm. After a batch of SLM parameter optimization, parameters for manufacturing specimens were: 300 W laser power, 500 mm/s scanning speed, 50 µm hatch spacing and 20 µm layer thickness. A chessboard scan strategy was employed with scan vectors rotated by 90º in adjacent 5 × 5 mm blocks and successive layers shifted by 1 mm in both X and Y direction. TNT5Zr-0.2 O alloy was obtained when perform in-situ alloying TNT5Zr due to the high oxygen affinity of the alloying elements, in addition to the use of high heat input parameters to ensure a homogenization melting of the alloying elements during SLM. The oxygen level in the SLM-manufactured alloy was measured using inert gas fusion standard test [14]. Among those as-fabricated samples, tensile specimen dimension was designed according to ASTM-E8/E8M-13a [15]; fatigue specimen was designed with tangentially blending fillets between the uniform test section and the ends according to ASTM-E466−15 [16]. The tensile and fatigue parts (10 mm in height) were horizontally manufactured with SLMed original side surface then sliced into dog-bone test-pieces (1.5 mm in height) by a wire electron discharge machining (EDM, GF Machining Solutions). Manual grinding kit (8220, Dremel) was used to reduce surface roughness of the fatigue test-pieces.

2.3. Advanced hot isostatic pressing

Besides achieving as-SLMed pores closure, advanced HIP (Quintus, Sweden) was used to tune the microstructure of TNT5Zr-0.2 O alloy. The investigated process parameters were: 3 h dwell at 1000 °C in a container filled with 120 MPa pressurized argon atmosphere, followed by different cooling processes, namely high cooling rate (1000 °C/min) and intermediate cooling rate (100 °C/min). The samples supplied for the advanced HIP treatment were three forms: cuboidal, tensile and fatigue test specimens.

2.4. Microstructure characterization

Metallographic specimens were prepared using automatic grinding and polishing (Tegramin 30, Struers), and then etched by Kroll's solution (2% HF + 6% HNO_3 + 92% H_2O). A field-emission gun (FEG) SEM (JSF-7000 F, JEOL) was used for observing the as-etched microstructure. The phase identification was performed by X-ray diffractometer (XRD) (AXRD, Proto) with Cu Kα radiation, and XRD spectra were collected by a fixed parameter of 0.02º step size and a 2 s time/step. Transmission electron microscopes (Talos F200X, FEI; Tecnai G2 F30, FEI) operating at 200 kV and 300 kV were used to capture bright-field (BF) TEM images & selected area diffraction (SAD) patterns, bright-field scanning transmission electron microscopy (BF-STEM) images, and high-angle annular dark-field (HAADF) images. Thin foils for TEM were prepared through an argon ion milling technique (Gatan PIPS, Ametek), involving gradient milling by different Ar ion energy and sputter angle settings.

2.5. Mechanical test

SLM-processed original side surface specimens (1.6 × 6 mm rectangular central cross-section) were used in tensile testing. And the tests were carried out perpendicularly to the build direction of as-fabricated samples at room temperature. The stress-strain curves
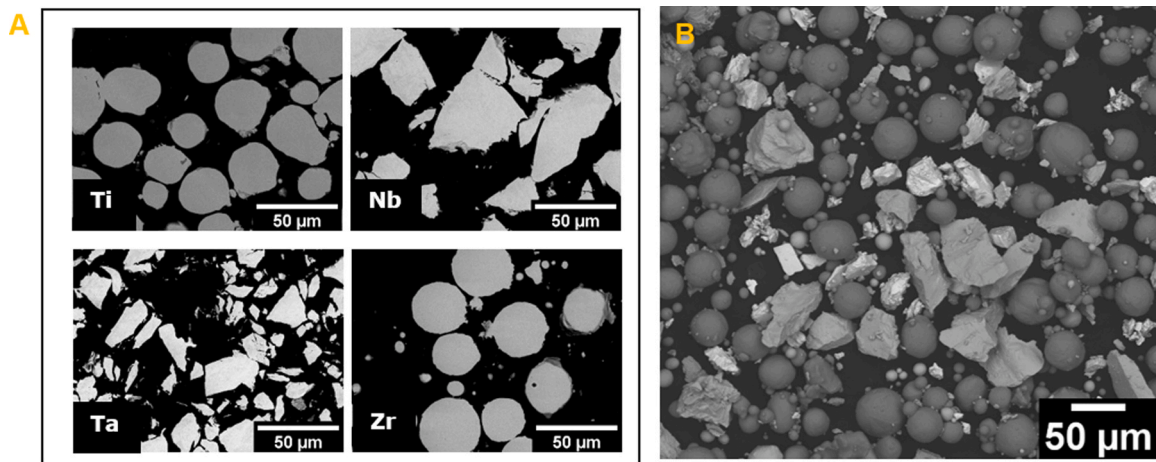
Fig. 1. (A) Cross-section micrographs of different pure element powders. (B) Particle morphology of blended TNT5Zr powder.

were measured at a crosshead speed of 0.5 mm/min at room temperature using a tensile testing machine (2500, Zwick/Roell). Two specimens per alloy were tested to compare tensile properties difference, and a clip-on extensometer was attached to 15 mm gauge length of specimen for strain measurement until rupture. Fatigue testing with rectangular central cross-section (1.5×6 mm) specimens were tested perpendicularly to the build direction. Axial high cycle fatigue testing was performed on a fatigue testing machine (Vibraphore Resonant), using magnetic resonance to deliver low constant amplitude (load ratio of R = 0.1), and 53 Hz high frequency (decided by the specimen geometry and stiffness). The testing with a maximum stress (up to 250 MPa) inside the elastic region was performed at room temperature. Tensile and fatigue fracture morphologies were observed using SEM (XL-30, Philips).

3. Results

3.1. Microstructure characterization

The XRD results for as-fabricated and as-HIPed TNT5Zr-0.2 O specimens are presented in Fig. 2. Single beta phase with $(110)_\beta$, $(200)_\beta$, and $(211)_\beta$ peaks were obtained in as-fabricated TNT5Zr-0.2 O alloy at room temperature. A profile of primary beta phase peaks along with low intensity α phase peak is revealed in TNT5Zr-0.2 O-
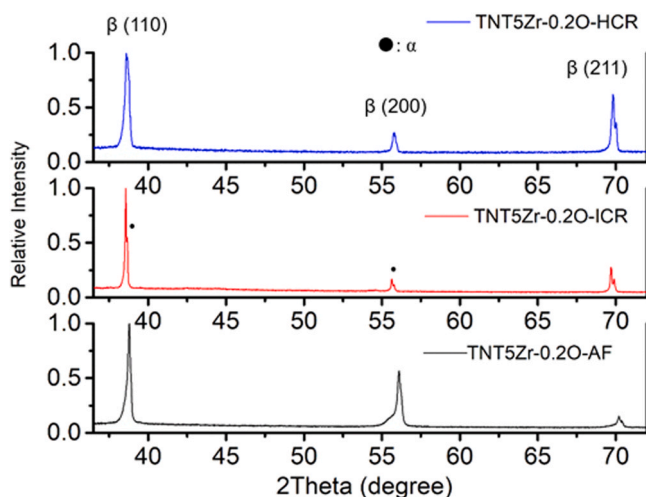

Fig. 2. X-ray diffraction patterns of the as-fabricated, as-HIPed (ICR), as-HIPed (HCR) TNT5Zr-0.2 O alloys. Note: $K_{\alpha 1}$ and $K_{\alpha 2}$ peak doublets are observed at high 2Theta angle.

ICR alloy, whereas TNT5Zr-0.2 O-HCR alloy only contains single β phase (Fig. 2).

Fig. 3 shows SEM images of microstructure captured from the as-fabricated, as-HIPed (ICR), as-HIPed (HCR) TNT5Zr-0.2 O alloys. Equiaxed β grains were obtained in TNT5Zr-0.2 O-AF alloy after performing in-situ alloying via SLM (Fig. 3A). The suspicious grain boundary alpha phase is observed in its high magnification (mag.) SEM micrograph (Fig. 3B). The same equiaxed grain type was kept in TNT5Zr-0.2 O-ICR alloy (Fig. 3C). At the same time, nucleation with discrete precipitates occurred at grain boundaries when the alloy was intermediately cooled from the 1000 °C HIP temperature (Fig. 3D). By comparison, TNT5Zr-0.2 O-HCR alloy retained equiaxed β grains in a manner without intragranular plate-like or acicular metastable precipitates after rapid cooling (Fig. 3E). In addition, no intergranular precipitates are seen in the corresponding high mag. SEM image (Fig. 3F).

TEM examination reveals grain matrices in TNT5Zr-0.2 O-AF and TNT5Zr-0.2 O-ICR alloy, as shown in the BF-TEM images (Fig. 4(A-B)); the corresponding SAD patterns (inset) taken from $[110]_\beta$ zone axis confirms the presence of single beta phase in grain matrices of both alloys. Similarly, BF-TEM micrograph taken from the beta grain matrix of TNT5Zr-0.2 O-HCR alloy, together with SAD pattern (Fig. 4C) reveals single beta phase without formation of metastable athermal precipitates. Fig. 4D demonstrates a BF-STEM image collected from grain boundary sites of TNT5Zr-0.2 O-ICR alloy. Clearly, heterogeneous discrete large plate-like precipitates nucleated and grew on grain boundaries. The corresponding grain boundary HAADF image and EDS maps of the involved elements (Ti, Nb, Ta, Zr, O) in TNT5Zr-0.2 O-ICR alloy are presented in Fig. 4E. The TEM-EDS analysis indicated the presence of secondary phases enriched in Ti element, leaned in Nb and Ta along grain boundary. Notably, parent beta phase appeared a uniform distribution of all the involved elements, and the existence of oxygen element were found in both two phases.

3.2. Tensile properties

The engineering stress-strain curves of as-fabricated and as-HIPed TNT5Zr-0.2 O alloys are given in Fig. 5. Table 1 summarizes the as-measured tensile properties including the former collected as-fabricated TNT5Zr alloy data (without oxygen pick-up) using the same testing method. Fig. 5 presents both the as-fabricated and as-HIPed (ICR) TNT5Zr-0.2 O alloy underwent elastic and plastic deformation till rupture. However, the as-HIPed (HCR) TNT5Zr-0.2 O alloy broke at the initial linear elastic region (682 ± 75 MPa) without yielding phenomenon. In the comparison with the obtained
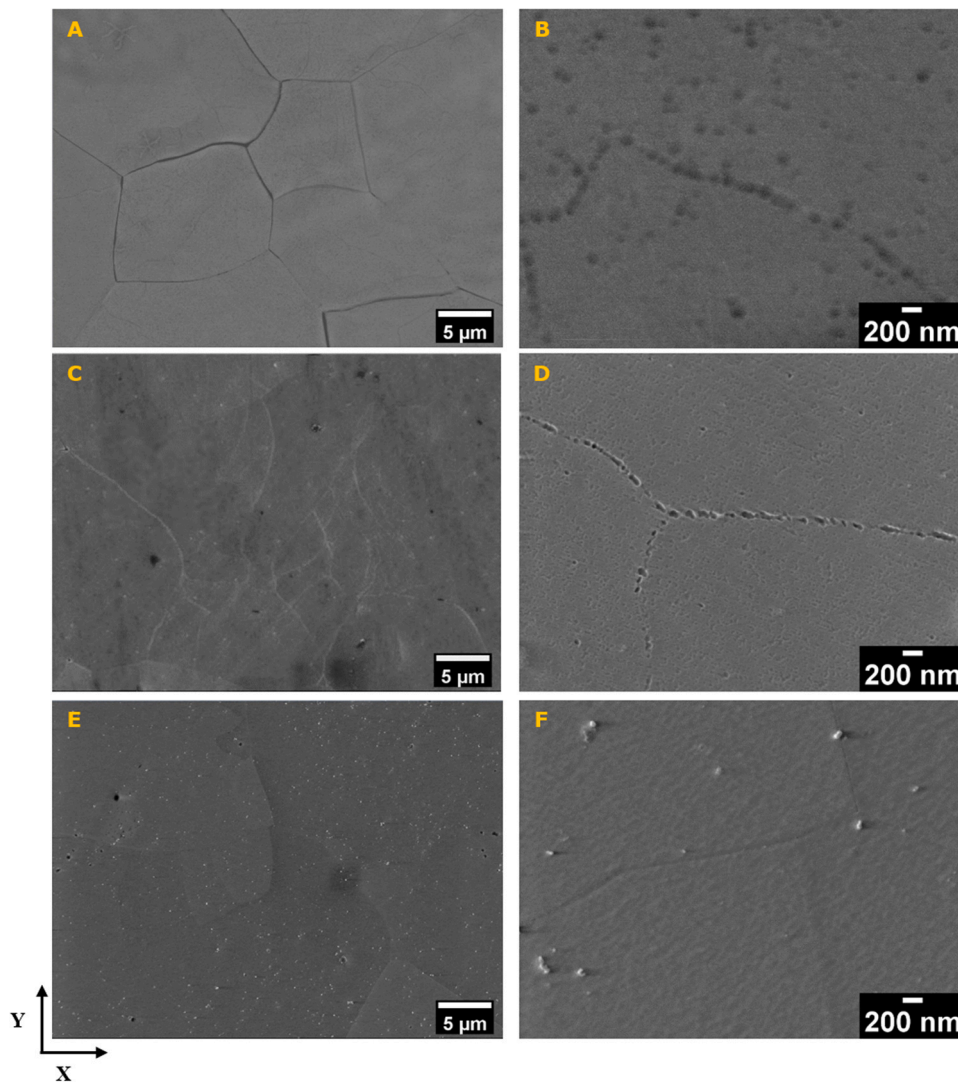
Fig. 3. (A) Low and (B) high mag. SEM micrographs illustrating the microstructure of as-fabricated TNT5Zr-0.2 O alloy; (C) low and (D) high mag. SEM micrographs illustrating the microstructure of TNT5Zr-0.2 O-ICR alloy; (E) low and (F) high mag. SEM micrographs illustrating the microstructure of TNT5Zr-0.2 O-HCR alloy.

mechanical data (Table 1), TNT5Zr-0.2 O-AF alloy possessed high ultimate tensile strength (UTS) of 975 ± 12 MPa, and elongation of 4.9% ± 0.3%; the TNT5Zr-0.2 O-ICR alloy obtained a slightly higher UTS (1036 ± 26 MPa) and lower elongation (3.0% ± 0.3%). When comparing tensile properties of TNT5Zr-0.2 O-AF and TNT5Zr-AF alloy, an obvious material strengthening with > 250 MPa UTS increase happened after oxygen pick-up during in-situ alloying via SLM. There appeared a slight elastic modulus (3 GPa in mean value) increase after absorption of oxygen in the as-fabricated alloy, and a further elastic modulus (9–15 GPa in mean value) rise after conducting two types of HIP treatment. Among these alloys, TNT5Zr-0.2 O-AF alloy obtained the highest σ_{UTS}/E ratio (16.3 ± 1.1) after the reinforcement effect caused by oxygen interstitial solutes and still maintained the low Young's modulus (60 ± 5 GPa).

Fig. 6 demonstrates representative fracture surfaces of TNT5Zr-0.2 O alloy at different conditions. The low mag. (Fig. 6 A) and intermediate mag. (Fig. 6B) SEM images show that the mixed surface of intergranular fracture together with intragranular fracture was found in TNT5Zr-0.2 O-AF alloy under tension. Meanwhile, high mag. (Fig. 6 C) fractograph reveals fine dimples at the central region of the ductile fracture. SEM images (Fig. 6(D-E)) of TNT5Zr-0.2 O-ICR alloy

fracture reveal a mixture of terrace-like intergranular fracture and matrix fracture formed by coalescence of voids; SEM fracture images (Fig. 6(G-H)) of TNT5Zr-0.2 O-HCR alloy demonstrates the flattest surface with intergranular/intragranular fracture. It is clearly found that low mag. fractographs (Fig. 6 (D, G)) show the absence of key-holes in the two as-HIPed TNT5Zr-0.2 O alloys; high mag. fractographs (Fig. 6(F, I)) show the two as-HIPed TNT5Zr-0.2 O alloys obtained the same dimple feature as TNT5Zr-0.2 O-AF alloy (Fig. 6 C) under tension.

3.3. Fatigue properties

Fig. 7 A shows the S-N curves of TNT5Zr-0.2 O-AF and TNT5Zr-0.2 O-ICR alloys obtained from plain fatigue test. Clearly, the fatigue limit of TNT5Zr-0.2 O-ICR alloy (150 MPa) is slightly higher than the counterpart of TNT5Zr-0.2 O-AF alloy (130 MPa). The number of cycles to failure in both alloys was almost the same in the maximum stress region (170–250 MPa). Low mag. SEM fractographs show fatigue crack preferably initiates from voids located in the surface of specimen in both alloys (Fig. 7(B-C)). These voids were kept after HIP treatment due to surface-connected pores cannot be removed if
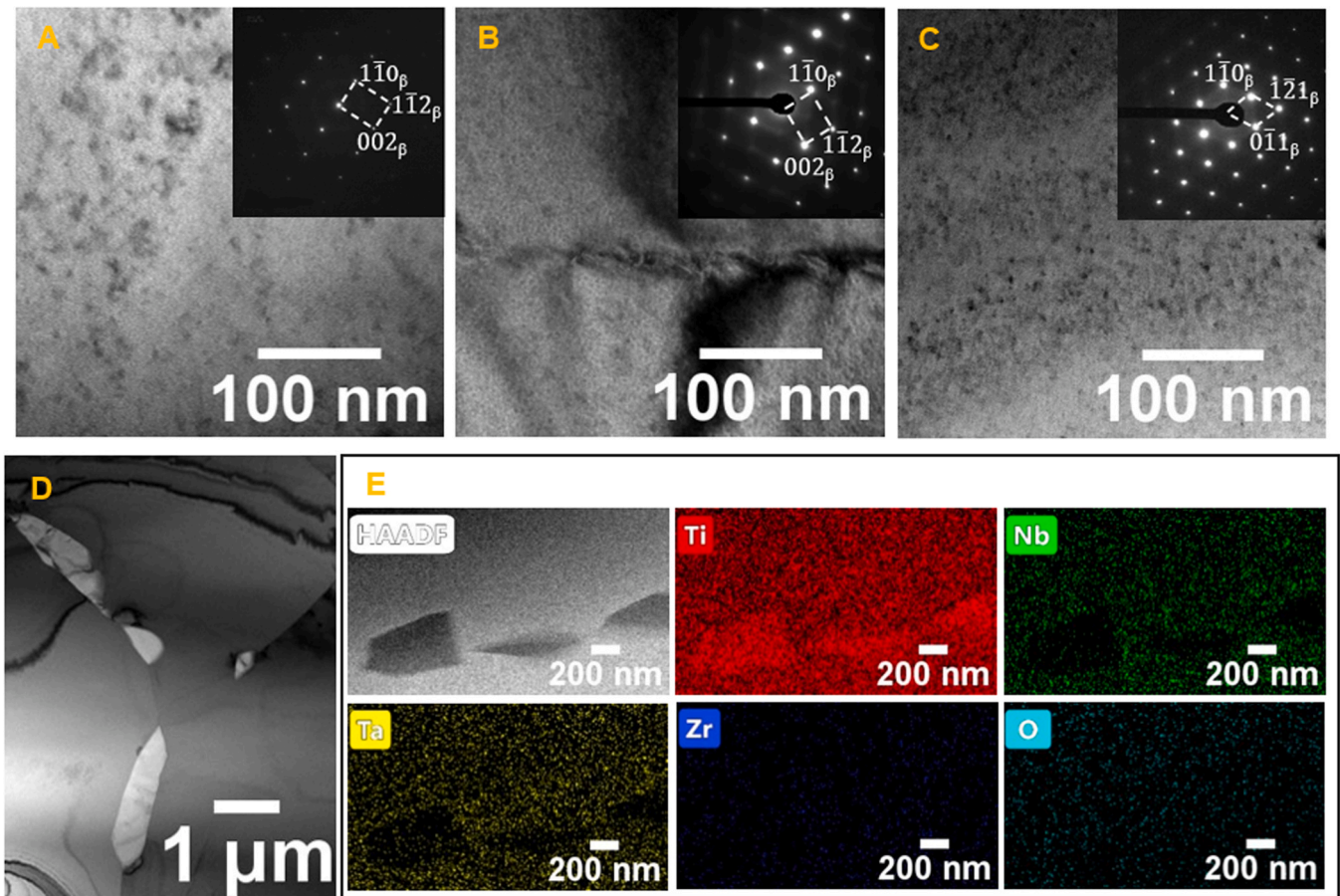
Fig. 4. (A) BF-TEM image collected from grain matrix with corresponding SAD pattern (inset) of TNT5Zr-0.2 O-AF, (B) TNT5Zr-0.2 O-ICR alloy, viewing from $[110]_\beta$ zone axis. (C) TNT5Zr-0.2 O-HCR alloy, viewing from $[111]_\beta$ zone axis. BF-STEM image of (D) TNT5Zr-0.2 O-ICR, taken from a region close to the grain boundary. (E) HAADF image captured from TNT5Zr-0.2 O-ICR grain boundary region and TEM-EDS distribution maps of Ti, Nb, Ta, Zr, O element. Note: the arrows showing the grain boundary sites.
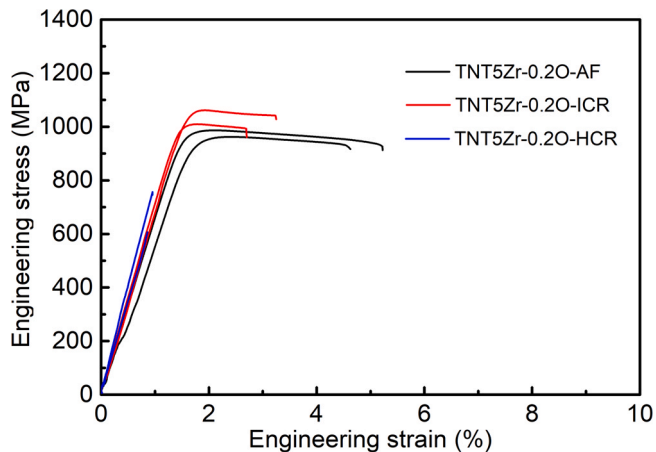

Fig. 5. Engineering stress-strain curves of as-fabricated and as-HIPed TNT5Zr-0.2 O alloys.

component is not coated or encapsulated, similarly reported by Atkinson et al. [21] and Williams et al. [22]. Three typical zones in TNT5Zr-0.2 O-AF alloy fatigue fracture surface, namely crack initiation, crack propagation and final fracture are revealed in Fig. 7(D-F). Under the uniaxial cyclic tensile stress, slip occurred on favorably orientated nearby planes in crack initiation site leads to the formation of crevices or intrusions and extrusions (Fig. 7D). Coarse slip band cracks combining appreciable striations are observed in the crack propagation zone (Fig. 7E) and fine dimples appear in the final fast fracture zone (Fig. 7 F), which demonstrates good ductility of the alloy. By comparison, slip-band cracking phenomenon with development of extrusion/intrusion pair is also observed in TNT5Zr-0.2 O-ICR alloy under cyclic loading (Fig. 7(G-H)). Unlike the typical fine cellular dimples found in the final fracture zone of TNT5Zr-0.2 O-AF (Fig. 7 F), intergranular and intragranular mixed fracture appears in TNT5Zr-0.2 O-ICR alloy (Fig. 7I). The discrete nano-sized grain boundary precipitates strengthened grain boundaries but at the same time locally high stress made there become the preferably fracture paths.

Table 1
Tensile properties of the SLM processed TNT5Zr, and TNT5Zr-0.2 O alloys subjected to different cooling rate HIP treatments.

Material	E (GPa)	$\sigma_{0.2}$ (MPa)	σ_{UTS} (MPa)	δ (%)	σ_{UTS}/E
TNT5Zr-0.2 O-AF	60 ± 5	938 ± 8	975 ± 12	4.9 ± 0.3	16.3 ± 1.1
TNT5Zr-0.2 O-ICR	69 ± 1	982 ± 6	1036 ± 26	3.0 ± 0.3	14.9 ± 0.7
TNT5Zr-0.2 O-HCR	75 ± 5	–	682 ± 75	0.9 ± 0.1	9.1 ± 0.4
TNT5Zr-AF [17]	57 ± 5	650 ± 8	698 ± 4	13.7 ± 0.6	12.1 ± 1.1
TNTZ [18–20]	46–80	447–900	545–950	–	–
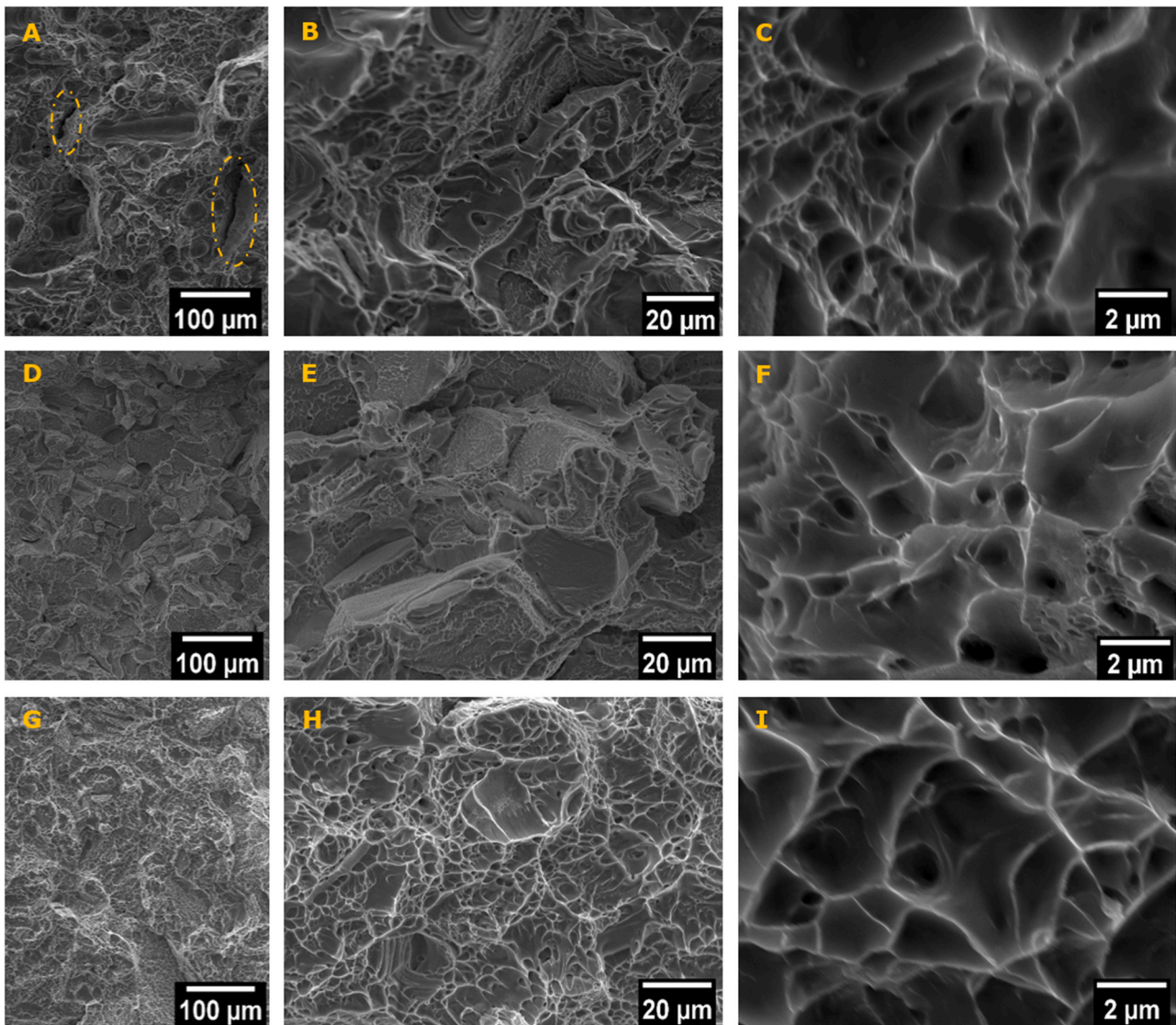
Fig. 6. (A), (B) and (C) increasing mag. SEM fractographs of as-fabricated TNT5Zr-0.2 O alloy; (D), (E) and (F) increasing mag. SEM fractographs of TNT5Zr-0.2 O-ICR alloy; (G), (H) and (I) increasing mag. SEM fractographs of TNT5Zr-0.2 O-HCR alloy. Note: the dash line zones in (A) show the deformed region located in keyhole.

4. Discussion

4.1. Microstructural evolution of the as-fabricated and as-HIPed β Ti alloys

Very small volume (below XRD detection limit) of nano-sized grain boundary alpha phases but no distinguishable precipitates within beta grain matrix can be seen in the as-fabricated TNT5Zr-0.2 O alloy when performing XRD, SEM and conventional TEM characterization. As oxygen concentration in Ti alloys has been found to raise the β transus temperature [23], which might provide more thermodynamic driving force and make precipitates more easily nucleate and grow along grain boundaries during TNT5Zr-0.2 O alloy solidification. In contrast to the prior work, similar XRD and TEM diffraction pattern belonging to single β phases were revealed in hot processing & solution treating, then quenching treated Ti-35 Nb-7Zr-5Ta-(0.06–0.68)O (wt%) alloys [24]. In TNT5Zr-0.2 O in-situ alloying, due to this β titanium alloy is constituted by enough β stabilizer elements (Nb, Ta), it obtained single beta grain matrix without formation of athermal ω and α'' phases even though the alloy underwent rapid cooling process in SLM. Therefore, the mechanism of oxygen suppressing athermal precipitates formation mentioned in

introduction section is not applicable to clarify findings in our work. Here, oxygen atoms occupied in the interstices of bcc β phase at sufficient concentration (0.8 at%) can well explain similar microstructure but pronounced tensile properties difference between the TNT5Zr-AF and TNT5Zr-0.2 O-AF alloys. The oxygen solid solute strengthening mechanism will be discussed later in 4.2 section.

TEM observation demonstrated the same single β phase within grain matrix in two as-HIPed TNT5Zr-0.2 O and as-fabricated TNT5Zr-0.2 O alloy (Fig. 4(A–C)). It observed that discrete large precipitates form along some grain boundaries in TNT5Zr-0.2 O alloy when subjected to intermediate cooling rate (100 °C/min) HIP treatment, captured by SEM (Fig. 3(C–D)). TEM characterization further confirmed that the presence of large Ti-rich grain boundary secondary phases (Fig. 4(D–E)), which is consistent with the element distribution in α phase found in Niinomi et al. [9] work. In the thermodynamic aspect of view, the usually heterogeneous formation of second-phase nucleus is favored at grain boundary sites of the parent phase. Because the energy barrier for heterogeneous nucleation is well lower than homogeneous nucleation, and the total Gibbs free energy is reduced by an increase of the nucleus size [25]. In our work, the magnitude of solute redistribution of Ti atoms from the matrix towards grain boundaries is moderately high at the HIP
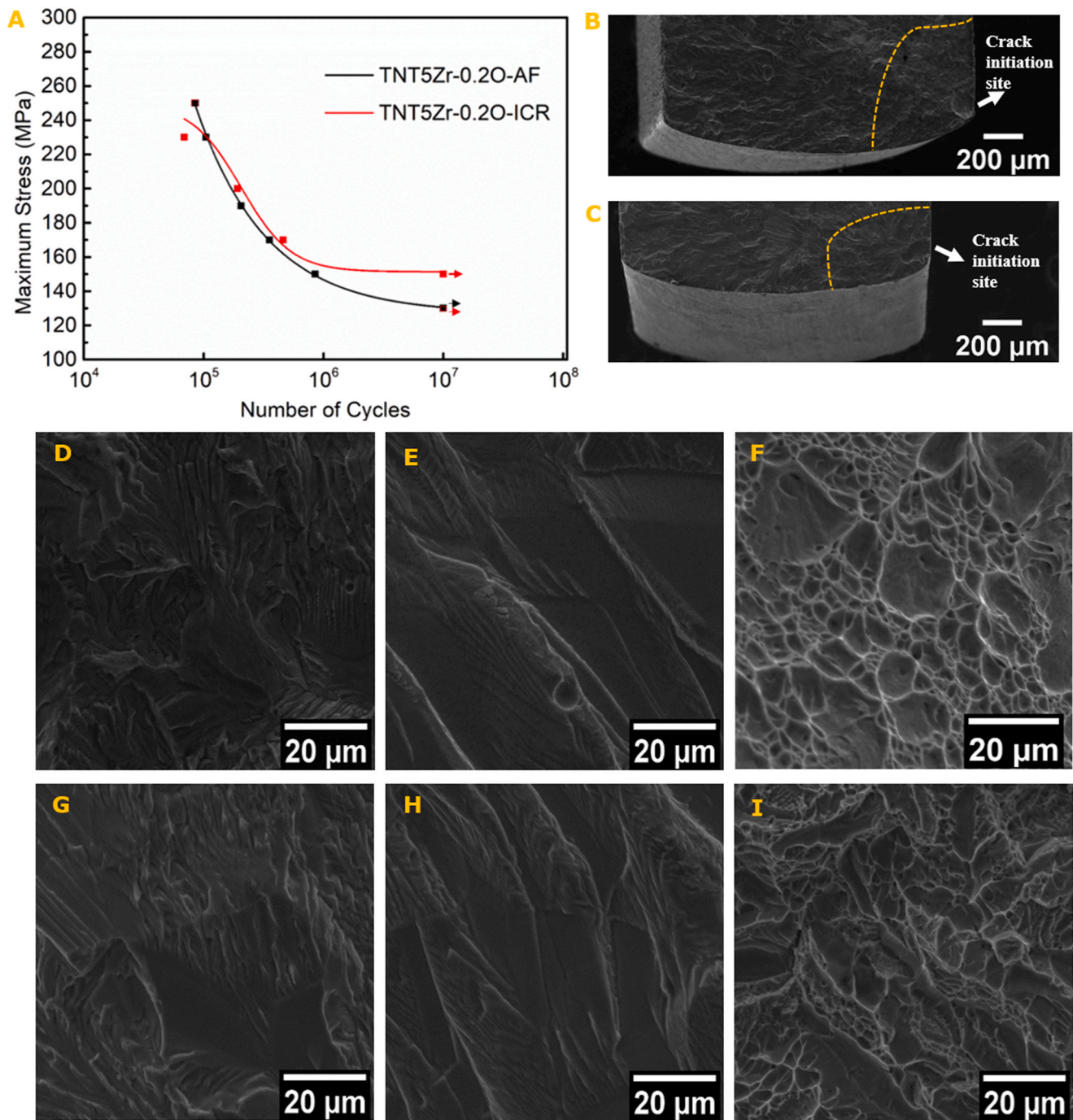
Fig. 7. (A) S-N curves of the as-fabricated and as-HIPed (ICR) TNT5Zr-0.2 O alloy. SEM morphology of (D) crack initiation area, (E) crack propagation area and (F) final fast fracture area of TNT5Zr-0.2 O-AF alloy. SEM morphology of (G) crack initiation area, (H) crack propagation area and (I) final fast fracture area of TNT5Zr-0.2 O-ICR alloy. Note: fatigue fracture surfaces were obtained from the maximum stress of 170 MPa. TNT5Zr-0.2 O-AF alloy failed at N = 354900; and TNT5Zr-0.2 O-ICR alloy, N = 460500. (B) Fatigue fracture illustrating both fatigue source and fatigue propagation zones taken from TNT5Zr-0.2 O-AF alloy, and (C) TNT5Zr-0.2 O-ICR alloy.

temperature (1000 °C). At the step of intermediate cooling, the intergranular precipitates possessed an ensuring solute concentration gradients and grain boundary diffusion coefficient for growth [26]. At the same time, second-phase particles tend to coalesce at high temperatures and form fewer large particles (Fig. 4D). Therefore, long-time high temperature heat treatment followed by slow cooling rate should be avoided due to the formation of detrimental coarse grain-boundary particles. By comparison, grain boundary alpha precipitates are fully suppressed in TNT5Zr-0.2 O-HCR alloy (Fig. 3(E–F)) because of much lower Ti element diffusion (from the

matrix to grain boundary) and nucleus growth rate when underwent high cooling rate (1000 °C/min) HIP.

4.2. Tensile properties of the studied alloys

Unlike the oxygen concentration control technique based on dissolution of titanium dioxide in conventional processing, the high oxygen-affinity of the involved elements (Zr, Ta, Nb, Ti) in SLM system make oxidation unavoidably occur at alloy melting and solidification stage. The strength enhancement after oxygen pick-up

during TNT5Zr in-situ alloying is found in our work (Table 1). A similar phenomenon was observed in solution treated Ti-35 Nb-7Zr-5Ta and Ti-24 Nb β-Ti alloys containing oxygen fabricated by conventional manufacturing [27,28]. The solution-hardening by oxygen was also found and clarified in pure α-Ti, Yu et al. [29] proposed that interstitial oxygen atoms move from the original sites into Ti basal planes due to the shear pronounced decreases the volume of hcp octahedral site. Additionally, the presence of oxygen atoms near the screw dislocation core may force part of dislocation to cross slip to the neighboring prismatic plane. Therefore, three factors, namely strong repulsion for oxygen and dislocation, large barriers for the "mechanical shuffle" of interstitial atoms in the core, and the local cross slip induced by oxygen atoms produce a strong pinning effect on screw dislocations. The scenario that cross-slip event induced by interstitial oxygen atom create two jogs on the screw dislocation is also seen in Zr-O alloys [30]. In addition, low Young's modulus (60 ± 5 GPa) was retained in our TNT5Zr-0.2 O-AF alloy due to its elastic deformation associated with bcc lattice structure stretching, which represents a big perturbation about the equilibrium spacing (more than 1% strain). We agree with the standpoint in Yang et al. work [31], the proper introduction of oxygen interstitial solutes in TNTZ-O alloy is an inexpensive, effective strengthening method for load-bearing implants manufactured by SLM. However, it will sacrifice materials' ductility if forms coarse grain boundary alpha precipitates.

Besides oxygen solid solute strengthening mechanism in TNT5Zr-0.2 O-ICR alloy, the nano-sized particles impede grain boundary migration and pin dislocation motion within the grain boundary. Normally, these particles preferentially appear at low-energy grain boundaries form pileup caused by interactions of the dislocations [32]. As a slightly higher UTS increase is observed in TNT5Zr-0.2 O alloy after HIP followed by 100 °C/min cooling, we presume that the pinning of planar dislocation has minor contribution on strength due to volume and size factor of the particles. Simultaneously, the UTS value of TNT5Zr-0.2 O-ICR alloy is also affected by the grain growth softening when it underwent 3 h dwell at 1000 °C. After comparing its fracture images (Fig. 6(D-F)) with the prior work, the mixed morphology in appearance of dimple-like transgranular fracture and brittle intergranular fracture is also found in Ti-28 Nb-13Zr-0.5Fe (wt%) specimen aged at 450 °C with the presence of grain boundary α precipitates [33].

The embrittlement phenomenon is seen in TNT5Zr-0.2 O alloy after HIP followed by 1000 °C/min cooling. Both residual stress and strain incompatibilities in anisotropic grains or grain boundaries may be relevant to brittleness of the alloy. As temperature of the surface and core of components is distinct in rapid cooling process, thermal residual stress may attain at room temperature [34]. The internal residual stress combining with the external loading make cracks proceed rapidly. At the same time, the strain incompatibilities in adjacent anisotropic grains produce locally high stresses near grain boundaries that could lead to crack initiation along boundaries under tension [35]. Moreover, the microvoids nucleate near the relatively weakened grain boundaries [36] without precipitation, then grow and coalesce into larger cavities when align with the low applied stress. It is noteworthy that unlike the conventional fracture of brittle material without significant plastic deformation, the dimpled intergranular fracture surfaces of TNT5Zr-0.2 O-HCR alloy (Fig. 6(G–I)) exhibit localized plasticity of the solute-strengthened beta grain matrix but a rapid collapse of grain boundary sites.

4.3. Fatigue characteristics of TNTZ-(O) alloys

Both TNT5Zr-0.2 O-ICR and TNT5Zr-0.2 O-AF alloy possessed low fatigue limit, namely 150 MPa and 130 MPa. Considering the porosity

factor, the resistance to fatigue is not markedly enhanced by removing the most of voids via HIP treatment. Due to the fatigue failure of the two alloys is determined by slip-band cracking mode, the cracks associated with slip band may take slightly shorter to propagate across the test-piece with voids. After a review of limited TNTZ alloy fatigue test results, many variable differences like material, geometry, testing condition (environment, frequency, etc.) can be found when making comparison with the as-measured values by Niinomi et al. [37] and Li et al. [38]. In the former study [37], the lowest fatigue limit (solution treated, mirror-like, 320 MPa) of the various heat-treated Ti-29 Nb-13Ta-4.6Zr alloys measured using rectangular-shaped flat plate test-pieces is much higher than our highest fatigue limit (ICR HIPed, grinded, 150 MPa) TNT5Zr-0.2 O alloy. Without considering microstructure difference, we presume that specimen surface finish, and geometry are the main factors to explain the marked gap of fatigue limits of these investigated TNTZ-(O) alloys. The notches like surface irregularities have been greatly eliminated after final polishing in Niinomi et al. [37] work, which reduced the fatigue crack initiation sites. At the same time, the rectangular-shaped geometry leads to less concentration of stress at the central region and provide a more uniform stress distribution along specimen. Both two advantages make the Ti-29 Nb-13Ta-4.6Zr alloys possessed much lower crack growth rate under cyclic deformation than TNT5Zr-0.2 O alloy.

5. Conclusions

This study investigated the microstructural evolution, mechanical properties of SLMed Ti-34 Nb-13Ta-5Zr-0.2 O alloy (TNT5Zr-0.2 O, wt%) before and after advanced HIP subjected to high and intermediate cooling rate (HCR & ICR). The main conclusions about the influence of oxygen concentration and cooling rate on microstructure and overall properties are drawn:

1. XRD analysis along with SEM and TEM micrographs reveal single beta phase in grain matrix of TNT5Zr-0.2 O-AF, TNT5Zr-0.2 O-ICR, TNT5Zr-0.2 O-HCR alloys. BF-STEM and HAADF micrographs show discrete large Ti-rich α precipitates formed along grain boundaries in TNT5Zr-0.2 O-ICR alloy. By comparison, grain boundary α particles are fully suppressed in TNT5Zr-0.2 O-HCR alloy.
2. TNT5Zr-0.2 O-AF alloy possessed high UTS of 975 ± 12 MPa, and elongation of 4.9% ± 0.3%; the TNT5Zr-0.2 O-ICR alloy shows slightly higher UTS (1036 ± 26 MPa) and lower elongation (3.0% ± 0.3%). However, TNT5Zr-0.2 O alloy breaks at the initial linear elastic region (682 ± 75 MPa) without yielding phenomenon. The mixed surfaces of intergranular fracture together with intragranular fracture are observed in these three alloys but appear an obvious grain boundary fracture morphology difference. Notably, TNT5Zr-0.2 O-AF alloy obtains the highest σ_{UTS}/E ratio (16.3 ± 1.1) and still maintains the low Young's modulus (60 ± 5 GPa).
3. S-N curves obtained from plain fatigue test show fatigue limit of TNT5Zr-0.2 O-ICR alloy (150 MPa) is slightly higher than the counterpart of TNT5Zr-0.2 O-AF alloy (130 MPa). SEM fractographs demonstrate fatigue crack preferably initiates from voids located in the surface of specimen, and slip-band cracking phenomenon with development of extrusion/intrusion pair is observed in both alloys.
4. The oxygen atoms occupied in the interstices of bcc β phase at sufficient concentration (0.8 at%), probably produce a strong pinning effect on screw dislocations. Therefore, the addition of proper amount oxygen interstitial solutes in TNTZ-O alloy is regarded as an inexpensive, effective strengthening technique for load-bearing biomedical applications.

CRediT authorship contribution statement

Weihuan Kong: Conceptualisation, Methodology, Investigation, Visualization, Validation, Formal analysis, Writing – original draft. **Elisabeth-Marie Francis:** Investigation (Transmission Electron Microscopy). **Qi Shi:** Investigation. **Sophie C. Cox:** Supervision. **Feng Wang:** Investigation. **Min Kuang:** Investigation (Hot isostsatic Pressing). **Moataz M. Attallah:** Conceptualisation, Methodology, Supervision, Resources, Investigation, Writing – review & editing.

Declaration of Competing Interest

The authors declare that they have no known competing financial interests or personal relationships that could have appeared to influence the work reported in this paper.

Acknowledgements

References

[1] M. Long, H.J. Rack, Titanium alloys in total joint replacement - a materials science perspective, Biomaterials (1998), https://doi.org/10.1016/S0142-9612(97)00146-4

[2] M. Tane, T. Nakano, S. Kuramoto, M. Hara, M. Niinomi, N. Takesue, T. Yano, H. Nakajima, Low Young's modulus in Ti-Nb-Ta-Zr-O alloys: cold working and oxygen effects, Acta Mater. (2011), https://doi.org/10.1016/j.actamat.2011.07.050

[3] M. Tane, T. Nakano, S. Kuramoto, M. Niinomi, N. Takesue, H. Nakajima, ω Transformation in cold-worked Ti-Nb-Ta-Zr-O alloys with low body-centered cubic phase stability and its correlation with their elastic properties, Acta Mater. (2013), https://doi.org/10.1016/j.actamat.2012.09.041

[4] L.S. Wei, H.Y. Kim, T. Koyano, S. Miyazaki, Effects of oxygen concentration and temperature on deformation behavior of Ti-Nb-Zr-Ta-O alloys, Scr. Mater. (2016), https://doi.org/10.1016/j.scriptamat.2016.05.043

[5] T. Saito, T. Furuta, J.H. Hwang, S. Kuramoto, K. Nishino, N. Suzuki, R. Chen, A. Yamada, K. Ito, Y. Seno, T. Nonaka, H. Ikehata, N. Nagasako, C. Iwamoto, Y. Ikuhara, T. Sakuma, Multifunctional alloys obtained via a dislocation-free plastic deformation mechanism, Science (2003), https://doi.org/10.1126/science.1081957

[6] K. Yokota, A. Bahador, K. Shitara, J. Umeda, K. Kondoh, Mechanisms of tensile strengthening and oxygen solid solution in single β-phase Ti-35 at%Ta+O alloys, Mater. Sci. Eng. A (2021), https://doi.org/10.1016/j.msea.2020.140677

[7] J. Wang, W. Xiao, L. Ren, Y. Fu, C. Ma, The roles of oxygen content on microstructural transformation, mechanical properties and corrosion resistance of Ti-Nb-based biomedical alloys with different β stabilities, Mater. Charact. (2021), https://doi.org/10.1016/j.matchar.2021.111122

[8] L. Umbelino dos Santos, K.N. Campo, R. Caram, É.S. Najar Lopes, Oxygen addition in biomedical Ti–Nb alloys with low Nb contents: effect on the microstructure and mechanical properties, Mater. Sci. Eng. A (2021), https://doi.org/10.1016/j.msea.2021.141750

[9] M. Niinomi, M. Nakai, M. Hendrickson, P. Nandwana, T. Alam, D. Choudhuri, R. Banerjee, Influence of oxygen on omega phase stability in the Ti-29Nb-13Ta-4.6Zr alloy, Scr. Mater. (2016), https://doi.org/10.1016/j.scriptamat.2016.06.027

[10] X. Tang, T. Ahmed, H.J. Rack, Phase transformations in Ti-Nb-Ta and Ti-Nb-Ta-Zr alloys, J. Mater. Sci. (2000), https://doi.org/10.1023/A:1004792922155

[11] R. Banerjee, S. Nag, J. Stechschulte, H.L. Fraser, Strengthening mechanisms in Ti-Nb-Zr-Ta and Ti-Mo-Zr-Fe orthopaedic alloys, Biomaterials (2004), https://doi.org/10.1016/j.biomaterials.2003.10.041

[12] S. Nag, R. Banerjee, H.L. Fraser, Microstructural evolution and strengthening mechanisms in Ti-Nb-Zr-Ta, Ti-Mo-Zr-Fe and Ti-15Mo biocompatible alloys, Mater. Sci. Eng. C (2005), https://doi.org/10.1016/j.msec.2004.12.013

[13] A. Najdahmadi, A. Zarei-Hanzaki, E. Farghadani, Mechanical properties enhancement in Ti-29Nb-13Ta-4.6Zr alloy via heat treatment with no detrimental effect on its biocompatibility, Mater. Des. (2014), https://doi.org/10.1016/j.matdes.2013.09.007

[14] E1409-13: Standard Test Method for Determination of Oxygen and Nitrogen in Titanium and Titanium Alloys by Inert Gas, Fusion, ASTM Stand, ASTM, 2013.

[15] ASTM E8, ASTM E8/E8M standard test methods for tension testing of metallic materials 1, Annu. B. ASTM Stand, 4, 2010. https://doi.org/10.1520/E0008.

[16] E466-15, Practice for conducting force controlled constant amplitude axial fatigue tests of metallic materials, ASTM B. Stand, 2015. https://doi.org/10.1520/E0466–15.2.

[17] W. Kong, S.C. Cox, Y. Lu, V. Villapun, X. Xiao, W. Ma, M. Liu, M.M. Attallah, The influence of zirconium content on the microstructure, mechanical properties, and biocompatibility of in-situ alloying Ti-Nb-Ta based β alloys processed by selective laser melting, Mater. Sci. Eng. C 131 (2021) 112486, https://doi.org/10.1016/J.MSEC.2021.112486

[18] D. Kuroda, M. Niinomi, M. Morinaga, Y. Kato, T. Yashiro, Design and mechanical properties of new β type titanium alloys for implant materials, Mater. Sci. Eng. A (1998), https://doi.org/10.1016/s0921-5093(97)00808-3

[19] J. Stráský, P. Harcuba, K. Václavová, K. Horváth, M. Landa, O. Srba, M. Janeček, Increasing strength of a biomedical Ti-Nb-Ta-Zr alloy by alloying with Fe, Si and O, J. Mech. Behav. Biomed. Mater. (2017), https://doi.org/10.1016/j.jmbbm.2017.03.026

[20] P. Laheurte, F. Prima, A. Eberhardt, T. Gloriant, M. Wary, E. Patoor, Mechanical properties of low modulus β titanium alloys designed from the electronic approach, J. Mech. Behav. Biomed. Mater. (2010), https://doi.org/10.1016/j.jmbbm.2010.07.001

[21] H.V. Atkinson, S. Davies, Fundamental aspects of hot isostatic pressing: an overview, Metall. Mater. Trans. A Phys. Metall. Mater. Sci. (2000), https://doi.org/10.1007/s11661-000-0078-2

[22] S. Tammas-Williams, P.J. Withers, I. Todd, P.B. Prangnell, The effectiveness of hot isostatic pressing for closing porosity in titanium parts manufactured by selective electron beam melting, Metall. Mater. Trans. A Phys. Metall. Mater. Sci. (2016), https://doi.org/10.1007/s11661-016-3429-3

[23] Z. Liu, G. Welsch, Effects of oxygen and heat treatment on the mechanical properties of alpha and beta titanium alloys, Metall. Trans. A (1988), https://doi.org/10.1007/BF02649267

[24] J.I. Qazi, B. Marquardt, L.F. Allard, H.J. Rack, Phase transformations in Ti-35Nb-7Zr-5Ta-(0.06-0.68)O alloys, Mater. Sci. Eng. C (2005), https://doi.org/10.1016/j.msec.2005.01.022

[25] L. Priester, Grain Boundaries: From Theory to Engineering, 2013. https://doi.org/10.1007/978–94-007–4969-6.

[26] M.V. Speight, Growth kinetics of grain-boundary precipitates, Acta Met. (1968), https://doi.org/10.1016/0001-6160(68)90081-3

[27] J.I. Qazi, V. Tsakiris, B. Marquardt, H.J. Rack, Effect of aging treatments on the tensile properties of Ti-35Nb-7Zr-5Ta-(0.06-0.7)O alloys, J. ASTM Int. (2005), https://doi.org/10.1520/jai12780

[28] A. Ramarolahy, P. Castany, F. Prima, P. Laheurte, I. Péron, T. Gloriant, Microstructure and mechanical behavior of superelastic Ti-24Nb-0.5O and Ti-24Nb-0.5N biomedical alloys, J. Mech. Behav. Biomed. Mater. (2012), https://doi.org/10.1016/j.jmbbm.2012.01.017

[29] Q. Yu, L. Qi, T. Tsuru, R. Traylor, D. Rugg, J.W. Morris, M. Asta, D.C. Chrzan, A.M. Minor, Origin of dramatic oxygen solute strengthening effect in titanium, Science (2015), https://doi.org/10.1126/science.1260485

[30] N. Chaari, D. Rodney, E. Clouet, Oxygen - dislocation interaction in zirconium from first principles, Acta Mater. (2017), https://doi.org/10.1016/j.actamat.2017.05.008

[31] P.J. Yang, Q.J. Li, W.Z. Han, J. Li, E. Ma, Designing solid solution hardening to retain uniform ductility while quadrupling yield strength, Acta Mater. (2019), https://doi.org/10.1016/j.actamat.2019.08.024

[32] P. Moretti, M.C. Miguel, M. Zaiser, S. Zapperi, Depinning transition of dislocation assemblies: pileups and low-angle grain boundaries, Phys. Rev. B Condens. Matter Mater. Phys. (2004), https://doi.org/10.1103/PhysRevB.69.214103

[33] W.F. Cui, A.H. Guo, Microstructures and properties of biomedical TiNbZrFe β-titanium alloy under aging conditions, Mater. Sci. Eng. A (2009), https://doi.org/10.1016/j.msea.2009.08.057

[34] P.J. Withers, H.K.D.H. Bhadeshia, Residual stress part 1 - measurement techniques, Mater. Sci. Technol. (2001), https://doi.org/10.1179/026708301101509980

[35] S. Lynch, A review of underlying reasons for intergranular cracking for a variety of failure modes and materials and examples of case histories, Eng. Fail. Anal. (2019), https://doi.org/10.1016/j.engfailanal.2019.02.027

[36] D.R. Askeland, The science and engineering of materials, Seventh ed., Cengage Learn, 2016.

[37] M. Niinomi, Fatigue performance and cyto-toxicity of low rigidity titanium alloy, Ti-29Nb-13Ta-4.6Zr, Biomaterials (2003), https://doi.org/10.1016/S0142-9612(03)00069-3

[38] S.J. Li, T.C. Cui, Y.L. Hao, R. Yang, Fatigue properties of a metastable β-type titanium alloy with reversible phase transformation, Acta Biomater. (2008), https://doi.org/10.1016/j.actbio.2007.09.009